MORB in the lowermost mantle beneath the western Pacific: Evidence from waveform inversion

Kensuke Konishi [a,*] , Kenji Kawai [b] , Robert J. Geller [a], Nobuaki Fuji [a]

[a] *Department of Earth and Planetary Science, Graduate School of Science, Tokyo University, Tokyo, Japan*

[b] *Department of Earth and Planetary Sciences, Tokyo Institute of Technology, Tokyo, Japan*

Abstract

We study the fine structure of the lowermost several hundred km of the large low shear velocity province (LLSVP) beneath the western Pacific by inverting the transverse components of long period (20-200 s) broadband seismic waveforms. We find a low S-velocity zone in the depth range from about 2550-2750 km, with the greatest decrease (relative to PREM) of about 0.2 km/s at depths of about 2650-2700 km. This suggests the presence of significant amounts of mid-ocean ridge basalt (MORB), for which the phase transitions from pv to ppv and from $CaCl_2$-type to α-PbO_2-type SiO_2 result in a decrease in S-velocities. We also find an increase in the S-velocity, relative to this minimum, of about 0.15 km/s, peaking in the depth range from about 2750-2800 km, which is consistent with the phase transition from pv to ppv expected for average composition models such as pyrolite.

Key words: waveform inversion, lowermost mantle, mid-ocean ridge basalt, pyrolite, phase transition

1 Introduction

Information on the lowermost layer of the mantle, called D″, under the western Pacific can help in elucidating important issues in geodynamics. Radiogenic isotopic variation in oceanic basalts indicates recycling of oceanic crust and primitive mantle reservoirs (Hofmann, 1997). The very high Pb isotopic ratios observed in some ocean island basalts, known as HIMU, support transport of MORB dehydrated in subduction zone (Kogiso et al., 1997). While many geochemists have favored models in which the mantle is chemically and dynamically layered with a depleted upper mantle and a primitive lower mantle, global models of 3-D mantle velocity structure obtained using seismic tomography suggest that subducted oceanic plates extend into the lower mantle (van der Hilst et al., 1997) and support whole mantle convection (Tackley, 2000). From a theoretical standpoint, the isotopic variation in oceanic basalt can be explained by whole mantle convection, and the possibility that MORB could descend into the lower mantle is suggested (Hirose et al., 1999; Xie and Tackley, 2004).

Tomographic studies (e.g., Grand, 2002) have shown that there is an LLSVP beneath the Central Pacific. Small-scale seismic scatterers that can be inter-

* Corresponding author.
Email addresses: ke-ko@eps.s.u-tokyo.ac.jp (Kensuke Konishi), kenji@geo.titech.ac.jp (Kenji Kawai), bob@eps.s.u-tokyo.ac.jp (Robert J. Geller), fuji@eps.s.u-tokyo.ac.jp (Nobuaki Fuji).

preted as MORB were observed at a depth of 1800 km northeast of the Mariana subduction zone (Kaneshima and Helffrich, 2003). A study of the LLSVP beneath the central Pacific suggested the existence of a MORB-enriched pile in this region (Ohta et al., 2008).

2 Methods

2.1 Waveform inversion

By systematically analyzing seismic waveforms recorded at many stations for many events as a single dataset, an improved Earth model can be obtained by minimizing the misfit between the data and the synthetic seismograms, subject to appropriate regularization. This procedure is called waveform inversion. Waveform inversion, which uses the full solution of the elastic equation of motion, is essentially akin to solving inverse scattering problems using physical optics, while travel-time tomography, which uses ray-theoretical approximations, is essentially akin to using geometrical optics.

Waveform inversion has been widely used (Mégnin and Romanowicz, 2000; Panning and Romanowicz, 2006; Takeuchi, 2007) to analyze surface-wave data for the structure of the upper mantle and transition zone, or to analyze global datasets for global 3-D Earth structure. However, waveform inversion of broadband body-wave data for the fine structure in a particular depth range beneath a particular geographic region is still relatively new (Kawai et al., 2007a,b). (We cite Kawai et al., 2007a, as KTGF07 below.) We use the methods of Kawai et al. (2006) to calculate the synthetic seismograms, and those of Geller and Hara (1993) to calculate the partial derivatives.

Waveform inversion can extract subtle information from an entire dataset, taken as a whole, that cannot be obtained by trial and error forward modeling of profiles for individual earthquakes. In this paper we present results of waveform inversion for a 1-D (S-velocity vs. depth) isotropic model, but our methods are formulated to also allow inversion for 3-D structure, anisotropy, and anelasticity.

Our procedures for data processing basically follow KTGF07; we briefly summarize them here. We use the transverse components of broadband waveform data obtained by rotating the N-S and E-W components. We apply a band-pass filter to construct a data set for the passband 0.005–0.05 Hz (i.e., for the period range, 20-200 s). A sampling rate of 1 Hz is used, and the instrument response is deconvolved. We account for structure outside the target region by making a static correction (time shift) as described by KTGF07. The source parameters (moment tensors and centroid) used to compute the synthetics are fixed to the Harvard CMT solutions. We approximate the moment rate function as a δ-function at the centroid time, which is an appropriate choice for the events and passband used in this study. In order to give all time windows the same importance, we use the reciprocal of the maximum amplitude in each time window as the weighting factor.

2.2 Data

In order to obtain waveforms that sample the target region, we mainly use waveforms of deep and intermediate-depth events beneath Tonga-Fiji and the Sea of Okhotsk that occurred between 1991 and 2006; we also use one event from the Aleutians (Fig. 1, Table 1). The data used in this study are observed

at epicentral distances from $69° < \Delta < 95°$. We used data from the following networks: F-net (obtained from the data center of the National Research Institute for Earth Science and Disaster Prevention of Japan), IRIS China (IC), IRIS/IDA (II), IRIS/USGS (IU) and the Ocean Hemisphere Project (OHP). A total of 1656 records which include data for S, ScS and the other phases which arrive between them were gathered. We then selected 483 records (ray-paths shown in Fig. 1) which met the data quality criteria of KTGF07 for use in this study.

2.3 Initial model

Since the existence of low S-velocities in the target region is well known (e.g., Grand, 2002) it is reasonable to expect that the velocity model for D″ in this region will differ substantially from PREM (Dziewonski and Anderson, 1981). We nevertheless begin by conducting an inversion using PREM as the starting model. The perturbation to the starting model is expressed as a linear combination of the eigenvectors corresponding to the n largest eigenvalues (Fig. 2) of the singular value decomposition (SVD) of the matrix of partial derivatives (see KTGF07 for details).

All of the resulting models (Fig. 3) show, as expected from tomography, an average velocity lower than PREM, but they all also show variation with depth, with the peak velocity in the depth range from about 2700-2800 km, and with lower velocities above and below this range. To address the question of whether this variation with depth is real or an artifact, we proceed as follows. We first define a new model, PREM′, as shown by the orange line in each panel of Fig. 3. PREM′ has roughly the average velocity found by our models in the

depth range 2500 km-CMB, and is tied into PREM at shallower depths. We then proceed to conduct inversion with respect to PREM′, as discussed below.

2.4 Inversions with respect to PREM′

In our inversions with respect to PREM′ we vary three parameters to examine the robustness of the inversion results. The first, which we call the 'tie-in depth,' is the depth above which the model is fixed to PREM′, with an S-velocity discontinuity allowed at the tie-in depth; we invert respectively for tie-in depths of 320, 360, and 400 km above the CMB. The second is the number of eigenvectors of the SVD used in the inversion; we invert for models using the eigenvectors corresponding to the first 3, 4, and 5 largest eigenvalues of the SVD decomposition, as the basis; these models are labelled SVD3, SVD4, and SVD5, respectively. Finally, we study the effect of the data selection criteria on the results. We use three data sets: (1) all 483 time windows ('all'), (2) the 440 records with a non-negative variance reduction (after the static correction) for model PREM′ ('Crit0'), and (3) the 319 records with a variance reduction of at least 30% (after the static correction) for model PREM′ ('Crit30').

The $3^3 = 27$ models obtained by the inversions varying the above parameters are shown in Fig. 4. PREM and PREM′ are also shown for reference. Fig. 4 shows that all of the models have basically the same general depth-dependence. There is a velocity decrease in the depth range 2600-2700 km and a relative velocity increase in the depth range 2700-2800 km. The velocity then decreases somewhat as the CMB is approached.

The inversions minimize the variance in the entire time window (which includes S and ScS). However, as the structure in D″ primarily affects ScS, we also compute the variance reduction for the ScS time window (Table 2). The upper three rows of Table 2 show the variance reduction for the full window, while the lower three rows show the results for the ScS window. The leftmost column in each row is the variance reduction for PREM, and the second column is the variance reduction for PREM′. The last nine columns of Table 2 are the variance reductions for each dataset for the respective tie-in depths and number of SVD eigenvectors. Further variance reduction (over PREM′) is obtained for all of the SVD inversions.

2.5 AIC

As an example, the variance reduction for the ScS window is 43.4% for PREM′, while it is 47.3% for SVD4 and a tie-in depth of 400 km. There might be some question of whether or not this 3.9% improvement in variance reduction is significant. The total number of data points (at 1 Hz sampling) in the full time windows is 53,638, 49,061, and 35,453 respectively for 'all,' 'Crit0,' and 'Crit30' respectively, and 28,574, 25,994, and 18,914 for the ScS windows. Since the data are filtered in the passband from 20 s to 200 s the effective number of independent data is 5% (1/20) of the above numbers of data points.

We use Akaike's Information Criterion (AIC) to confrm the significance of the variance reduction data shown in Table 2. AIC is defined as follows (Akaike, 1977):

$$\begin{aligned} AIC(k) &= -2(\text{Maximum Log-Likelihood}) + 2k \\ &= n \log 2\pi + n \log \sigma^2 + n + 2k, \end{aligned} \tag{1}$$

where k is the number of free parameters (the number of unknown coefficients plus one, where one is added because the variance of the residuals is another unknown); n is the number of data (5% of the total number of points in the respective time series, as discussed above), and σ^2 is the variance of the residuals. AIC gives an unbiased estimate of the mean log-likelihood of the model for a given data set. AIC in effect penalizes an increase in the number of model parameters by requiring that a commensurate improvement in the variance reduction must be achieved before a more complex model can be accepted as meaningful. Table 3 shows the AIC value for each dataset for PREM$'$ and for the nine corresponding SVD inversions. All of the inversions yield a lower value of AIC than that for PREM$'$, which confirms the statistical significance of the variance reduction achieved by the SVD inversions.

2.6 Static corrections

Another possible question is the effect of the time shifts ('static corrections'). To address this question we also conducted inversions relative to PREM$'$ without making any time shifts. A data set of 303 time windows with a variance reduction of 30% (relative to synthetics for PREM$'$ when no time shift was made) was used, and the resulting models for SVD3 and SVD4 are shown beneath the dotted line in Fig. 4. The models obtained have essentially the same character as the models obtained by the actual inversions, except that the absolute velocities are systematically shifted to lower values. Thus we conclude that the pattern of depth dependence of the velocity models is not an artifact of the time shifting, but that hypothetical errors in the time shifting procedure might cause small errors in the absolute velocities.

2.7 Synthetic resolution tests

We conduct synthetic resolution ('checkerboard') tests to examine the ability of our methods to resolve various synthetic structure models. We conducted tests for four model perturbations (Fig. 5). Synthetic seismograms were calculated exactly for these four models and then used as the input for inversions relative to PREM′. As shown in Fig. 5 the input models could be recovered satisfactorily, although not perfectly.

2.8 Stacked waveforms

Previous researchers have conducted waveform modeling by visual trial-and-error matching of the data and synthetics for individual earthquakes, whereas we conduct waveform inversion by quantitive and objective comparsion of a dataset of seismograms for many earthquakes. The latter is clearly preferable from the general standpoint of data analysis methods in physical science, but some researchers may harbor doubts because it is a 'black-box' procedure. We address such hypothetical doubts by presenting stacked waveforms for the ScS time window for the six events with the largest number of waveforms (Fig. 6). The stacked waveforms are plotted with the black (data) on bottom, overlayed in turn by the blue (PREM), green (PREM′) and orange (final model) traces. We choose the SVD4 inversion for the 'Crit30' dataset with a tie-in depth of 400 km as the final model for the stacks. When one or more traces match, only the top trace is visible in Fig. 6. As suggested by Fig. 6, the model obtained by waveform inversion is more successful in explaining the waveform data for the ScS window than PREM′ or PREM.

To further illustrate the way in which the variance is reduced by the inversion we consider the upper right box of Fig. 6 (the stack for event 20050319), which we shown in detail in Fig. 7. Fig. 7 shows the stack of the observed data (OBS), the stacked synthetics for the starting model (PREM′) and the successive stacks as the components corresponding to the first, second, . . . , fifth eigenvectors are added to the synthetics. The amplitude of each of these components in the model space is shown by the histogram in the inset. The plot is made with the traces for SVD5 overlain by those for SVD4, and so on. As we progress from the stacked synthetics for PREM′ to those for SVD4, it is clear that the first peak is shifted successively to the right (later), while the second is shifted successively to the left (earlier), which in both cases improves the fit. Such a subtle shift would not necessarily be believable if it were obtained by trial and error fitting of one stack at a time, but this is actually a result that was obtained by a systematic inversion of several hundred high quality waveforms, and the stacks are presented only for confirmative purposes. This is thus an illustration of the power of waveform inversion.

2.9 Model uncertainty

It is desirable to obtain estimates of the uncertainty of our models. However, as is well known, such error estimates are always lower bounds on the true uncertainty, as they do not reflect parameters and effects not included in the modeling. We estimate the uncertainties in three different ways (Fig. 8). In the left panel we take nine models (three each for SVD3, SVD4, and SVD5) from the three panels of Fig. 3 (inversions with respect to PREM), and plot

their average (center trace) and the standard deviations ($\pm 1\sigma$) obtained by formally treating them as independent data (left and right traces). In the center panel we use the same display format as the left panel for the 27 models (SVD3-SVD5) in the uppermost nine panels of Fig. 4. In the right panel we plot the standard deviation for the model in the center panel in the third row of Fig. 4, obtained using a statistical propagation-of-errors analysis. If taken at face value the results in Fig. 8 suggest uncertainties of about $0.05 - 0.1$ km/s, which is considerably smaller than the difference between the lowest velocities (at depths of about 2700 km) and the highest velocities (at depths of about 2800 km), and is also consistent with the AIC results which show that the SVD3-SVD5 models in Fig. 4 all represent a statistically significant improvement over PREM′.

3 Discussion

It has been suggested (e.g., Tackley, 1998) that D″ in the LLSVP beneath the Pacific is chemically distinct from D″ in other regions due to dense debris of subducted oceanic slabs, which accumulated when the Rodinia supercontinent was created (Maruyama et al., 2007). The remnants of dense MORB crust which includes Al- and Fe-rich Mg-perovskite and $CaCl_2$-type SiO_2 are thus expected to have accumulated in D″ beneath the Pacific (e.g., Christensen and Hofmann, 1994).

In this paper we studied the fine structure of D″ in the northwestern part of the LLSVP. We found an "S-shaped model" (Fig. 4) with 1.5-2% velocity decreases and increases in the zones from 200-300 km and from 100-200 km above the CMB, respectively. The velocity decrease can be interpreted as

due to the phase transitions in MORB from Mg-pv to Mg-ppv (Tsuchiya and Tsuchiya, 2006) and from $CaCl_2$-type to α-PbO_2-type SiO_2 (Karki et al., 1997), and the velocity increase can be interpreted as due to the phase transition in pyrolite from pv to ppv (Tsuchiya et al., 2004). The velocity decrease and increase occur in a depth range of about 100 km, which is a 6 GPa pressure range. This is consistent with experimental results for phase relations in pyrolite and MORB (Ohta et al., 2008). Therefore, the obtained model suggests that a mixture of MORB and pyrolitic materials exist in this region (although a chemically heterogeneous model cannot be excluded). The occurrence of the inferred phase transitions from pv to ppv over a depth range of 100 km may be due to solution of Al and Fe.

A question remains about the velocity structure in the depth range between about 2800 km and the CMB. In our work on the velocity structure beneath central America (Kawai et al., 2007a) and the Arctic (Kawai et al., 2007b) we found evidence of a double crossing phase transition near the CMB (i.e., a velocity decrease near the CMB interpreted as being due to a reverse phase transition from ppv back to pv due to the high temperature gradient). Since the CMB should be isothermal, thermodynamic arguments (Hernlund et al., 2005) suggest that double crossing phase transitions could also be expected in our study region. Our models (Fig. 4) are consistent with the possible existence of reverse phase transitions from ppv back to pv near the CMB, but we lack the resolution to definitely establish their existence.

Our results were obtained by inversion of broad-band body-wave waveforms. Waveform inversion, as well as other quantitative inversion techniques (e.g. van der Hilst et al., 2007), allows robust determination of the fine structure of seismic velocities, and we expect that the applications of such techniques will

continue to contribute to our knowledge of Earth structure.

4 Acknowledgments

We thank Kei Hirose, Shigenori Maruyama, David Yuen, Tatsuhiko Hara and Hiromitsu Mizutani for variable suggestions and comments. Data were obtained from the NIED F-net, IRIS, and OHP data servers. This research was partly supported by grants from the Japanese Ministry of Education, Science and Culture (No. 19740272). NF is supported by a JSPS Fellowship for Young Scientists.

References

Akaike, H., 1977. Extension of method of maximum likelihood and the Stein's problem. Annals of the Institute of Statistical Mathematics 29, 153–164.

Christensen, U.R., Hofmann, A.W., 1994. Segregation of subducted oceanic-crust in the convecting mantle. J. Geophys. Res. 99, 19867–19884.

Dziewonski, A.M., Anderson, D.L., 1981. Preliminary reference Earth model. Phys. Earth Planet. Inter. 25, 297–356.

Geller, R.J., Hara, T., 1993. Two efficient algorithms for iterative linearized inversion of seismic waveform data. Geophys. J. Int. 115, 699–710.

Grand, S.P., 2002. Mantle shear-wave tomography and the fate of subducted slabs. Phil. Trans. R. Soc. A 360, 2475–2491.

Hernlund, J.W., Thomas, C., Tackley, P.J., 2005. A doubling of the post-perovskite phase boundary and structure of the Earth's lowermost mantle. Nature 434, 882–886.

van der Hilst, R.D., Widiyantoro, S., Engdahl, E.R., 1997. Evidence for deep mantle circulation from global tomography. Nature 386, 578–584.

van der Hilst, R.D., de Hoop, M.V., Wang, P., Shim, S.H., Ma, P., Tenorio, L., 2007. Seismostratigraphy and thermal structure of Earth's core-mantle boundary region. Science 315, 1813-1817.

Hirose, K., Fei, Y., Ma, Y., Mao, H., 1999. The fate of subducted basaltic crust in the Earth's lower mantle. Nature 397, 53-56.

Hofmann, A.W., 1997. Mantle geochemistry: the message from oceanic volcanism. Nature 385, 219–229.

Kaneshima, S., Helffrich, G., 2003. Subparallel dipping heterogeneities in the mid-lower mantle. J. Geophys. Res. 108, 2272, doi:10.1029/2001JB001596.

Karki, B.B., Stixrude, L., Crain, J., 1997. Ab initio elasticity of three high-

290 pressure polymorphs of silica. Geophys. Res. Lett. 24, 3269–3272.
291 Kawai, K., Takeuchi, N., Geller, R.J., 2006. Complete synthetic seismograms
292 up to 2 Hz for transversely isotropic spherically symmetric media. Geophys.
293 J. Int. 164, 411–424.
294 Kawai, K., Takeuchi, N., Geller, R.J., Fuji, N., 2007a. Possible evidence
295 for a double crossing phase transition in D″ beneath Central America
296 from inversion of seismic waveforms. Geophys. Res. Lett. 34, L09314,
297 doi:10.1029/2007GL029642.
298 Kawai, K., Geller, R.J., Fuji, N., 2007b. D″ beneath the Arctic from inversion
299 of shear waveforms. Geophys. Res. Lett. 34, doi:10.1029/2007GL031517.
300 Kogiso, T., Tatsumi, Y., Nakano, S., 1997. Trace element transport during
301 dehydration processes in the subducted oceanic crust: 1. Experiments and
302 implications for the origin of ocean island basalts. Earth Planet. Sci. Lett.
303 148, 193–205.
304 Maruyama, S., Santosh, M., Zhao, D.P., 2007. Superplume, supercontinent,
305 and post-perovskite: Mantle dynamics and anti-plate tectonics on the core-
306 mantle boundary, Gondowana Res. 11, 7–37.
307 Mégnin, C., Romanowicz, B., 2000. The three-dimensional shear velocity
308 structure of the mantle from the inversion of body, surface and higher-mode
309 waveforms. Geophys. J. Int. 143, 709–728.
310 Ohta, K., Hirose, K., Lay, T., Sata, N., Ohishi, Y., 2008. Phase transitions
311 in pyrolite and MORB at lowermost mantle conditions: Implications for a
312 MORB-rich pile above the core-mantle boundary. Earth Planet. Sci. Lett.
313 267, 107–117.
314 Panning, M., Romanowicz, B., 2006. A three-dimensional radially anisotropic
315 model of shear velocity in the whole mantle. Geophys. J. Int. 167, 361–379.
316 Tackley, P.J., 1998. Three-dimensional simulations of mantle convection with a

thermo-chemical basal boundary layer: D″? in *The Core-Mantle Boundary Region* (eds. Gurnis, M., Wysession, M.E., Knittle, E. and Buffet, B.A.) Geodyn. Ser., vol. 28. American Geophysical Union, Washington, DC, 231–253.

Tackley, P.J., 2000. Mantle convection and plate tectonics: Toward an integrated physical and chemical theory. Science 288, 2002–2007.

Takeuchi, N., 2007. Whole mantle SH velocity model constrained by waveform inversion based on three-dimensional Born kernels. Geophys. J. Int. 169, 1153–1163.

Tsuchiya, T., Tsuchiya, J., Umemoto, K., Wentzcovitch, R.A., 2004. Phase transition in $MgSiO_3$ perovskite in the earth's lower mantle. Earth and Planet. Sci. Lett. 224, 241–248.

Tsuchiya, T., Tsuchiya, J., 2006. Effect of impurity on the elasticity of perovskite and postperovskite: Velocity contrast across the postperovskite transition in $(Mg,Fe,Al)(Si,Al)O_3$, Geophys. Res. Lett. 33, L12S04, doi:10.1029/2006GL025706.

Xie, S., Tackley, P.J., 2004. Evolution of U-Pb and Sm-Nd systems in numerical models of mantle convection and plate tectonics. J. Geophys. Res. 109, B11204, doi:10.1029/2004JB003176.

Fig. 1. Event-receiver geometry, with great circle ray paths. The portions of the great circles which sample D″ are shown in red; plus signs indicate the turning points within D″. Blue triangles show the stations, and red stars show the earthquakes.

Fig. 2. (Top) The first fifteen eigenvalues of the singular value decomposition (SVD) for the PREM′ model with a tie-in depth located 400 km above the CMB, with the largest eigenvalue normalized to one. (Bottom) The eigenvectors for the five largest eigenvalues. The eigenvalues and eigenvectors for PREM differ only slightly from those shown in this figure.

Fig. 3. The results of the various inversions with respect to PREM. The left, center and right panels are for tie-in depths of 320, 360, and 400 km above the CMB, respectively. Each panel shows results for five inversions (using the eigenvectors for the first 1, 2, 3, 4 and 5 largest eigenvalues respectively). The inversion result for the single eigenvector basis is plotted as a thick curve. The red line shows PREM′, which we use as the initial model in our further inversions.

Fig. 4. The results of the various inversions. Each panel shows results for three inversions, in which the tie-in depths are set to 320, 360, and 400 km above the CMB, respectively. PREM and PREM′ are also plotted as dotted lines in each panel. The three columns, from left to right, are for inversions using the eigenvectors for the first three, four, and five largest eigenvalues as the basis, respectively. The top row is an inversion using all 483 waveforms. The second row uses a data set ('Crit0') in which the 43 records with a negative variance reduction for PREM′ are eliminated, and the third row uses a data set ('Crit30') in which 164 records with a variance reduction of less than 30% for PREM′ are eliminated. In all cases essentially similar models are obtained, supporting the robustness of the results of waveform inversion. The two panels below the dotted line are inversions of 301 records with a variance reduction of 30% or better relative to synthetics for PREM′ when no time shift is made. The same general pattern is obtained, but the models are somewhat slower than the actual inversion results.

Fig. 5. Resolution test for D″ structure (details in text). The red lines are the input model. The black curves are the inversions with respect to PREM′ for the various tie-in depths. The inversions reasonably recover the starting models.

Fig. 6. Stacked waveforms (data and synthetics) are presented to provide a general visual illustration of the fits of the data and waveforms for the various models. N is the number of waveforms in each stack. The post-inversion model (MODEL) used in these stacks is the center box in the third ('Crit30') row of Fig. 4 for a tie-in depth of 400 km. Although stacks are aligned to the S-wave arrival time , we show the traces from the ScS-wave arrival time (leftmost arrow). The numbers shown for each set of synthetics means the average variance reduction for the ScS window.

Fig. 7. We consider the upper right box of Fig. 6 (the stack for event 20050319) in detail. This figure shows the stack of the observed data (OBS), the stacked synthetics for the starting model (PREM′), and the successive stacks as the components corresponding to the first, second, ..., fifth eigenvectors are added to the synthetics. The amplitude of each of these components in the model space is shown by the histogram in the inset. The plot is made with the traces for SVD5 overlain by those for SVD4, and so on. As we progress from the stacked synthetics for PREM′ to those for SVD4, the first peak is shifted successively to the right (later), while the second is shifted successively to the left (earlier), which in both cases improves the fit.

Fig. 8. Three different estimates of the model uncertainty. (Left panel) We take nine models (three each for SVD3, SVD4, and SVD5) from the three panels of Fig. 3 (inversions with respect to PREM), and plot their average (center trace) and the standard deviations ($\pm 1\sigma$) obtained by formally treating them as independent data. (Center panel) Same display format as the left panel, for the 27 models (SVD3-SVD5) in the uppermost nine panels of Fig. 4. (Right panel) Standard deviation for the model in the center panel in the third row of Fig. 4, obtained using a statistical propagation-of-errors analysis.

Event#	Y/M/D	Lat	Long	Depth	M_w
1	1991/7/5	47.96	145.91	465.2	5.8
2	1994/8/2	52.40	158.27	159.3	5.8
3	1997/12/20	53.40	152.71	622.9	5.9
4	1999/2/5	47.47	147.73	402.4	5.8
5	2000/7/10	46.83	145.59	361.3	5.8
6	2001/2/26	46.79	144.54	396.4	6.0
7	2001/4/28	-18.07	-176.68	367.4	6.8
8	2001/5/26	-20.25	-177.65	413.9	6.3
9	2001/10/3	46.95	148.62	288.1	5.9
10	2001/11/5	-17.12	-178.96	579.7	6.2
11	2002/1/2	-17.63	178.84	680.8	6.1
12	2002/8/9	-16.25	-175.85	381.3	6.1
13	2002/10/17	-19.80	-178.23	621.9	6.1
14	2002/12/10	-24.02	179.28	538.8	6.0
15	2003/1/4	-20.72	-177.32	394.7	6.5
16	2003/3/14	-17.50	-174.77	282.4	6.3
17	2003/6/16	55.48	160.25	180.9	6.9
18	2004/6/10	55.79	160.32	190.1	6.8
19	2004/11/7	47.93	144.52	493.0	6.1
20	2004/12/28	53.18	-173.79	258.4	5.8
21	2005/3/19	-21.88	-179.27	609.2	6.3
22	2005/8/6	-19.60	-175.35	217.7	6.0
23	2006/1/2	-19.80	-177.72	589.5	7.2
24	2006/2/2	-17.77	-178.13	611.6	6.7
25	2006/2/24	-17.94	-179.42	640.9	6.1
26	2006/2/26	-23.59	-179.82	553.9	6.4
27	2006/5/22	54.19	158.87	198.0	6.2
28	2006/6/2	-20.77	-178.54	584.6	6.0
29	2006/6/9	-17.36	-178.62	585.9	6.1

Table 1
Earthquakes used in this study.

	PREM	PREM′	320 km			360 km			400 km		
			3	4	5	3	4	5	3	4	5
Full											
all	22.4	32.6	33.7	33.8	33.8	33.9	33.9	33.9	33.9	33.9	33.9
Crit0	29.3	39.4	40.1	40.1	40.1	40.1	40.1	40.1	40.0	40.1	40.1
Crit30	38.4	47.4	47.7	47.8	47.8	47.7	47.8	47.8	47.6	47.8	47.8
ScS											
all	2.6	26.8	32.7	32.8	33.0	32.2	31.8	32.1	31.2	31.3	31.5
Crit0	8.43	32.9	38.5	38.5	38.7	37.8	38.2	38.3	36.2	38.1	38.3
Crit30	19.5	43.4	47.1	47.2	47.2	46.7	47.2	47.1	45.5	47.3	47.4

Table 2
Variance reduction(%) for each model.

	PREM′	320 km			360 km			400 km		
		3	4	5	3	4	5	3	4	5
Full										
all	3907.0	3869.8	3868.7	3871.2	3862.8	3865.1	3867.2	3862.8	3864.5	3866.5
Crit0	3348.9	3322.9	3324.8	3327.0	3322.6	3323.7	3325.7	3327.9	3323.9	3325.9
Crit30	2200.9	2192.1	2193.6	2195.6	2193.0	2193.6	2195.4	2196.2	2193.8	2195.9
ScS										
all	2185.7	2082.4	2079.1	2075.5	2090.3	2100.1	2096.5	2109.0	2108.6	2107.5
Crit0	1890.0	1791.3	1793.4	1793.0	1804.9	1799.7	1800.3	1833.8	1800.9	1800.2
Crit30	1236.4	1181.2	1181.9	1184.2	1188.2	1181.6	1185.1	1205.5	1179.8	1181.3

Table 3
AIC for each model.

Figure
Click here to download Figure: newfigures4.pdf

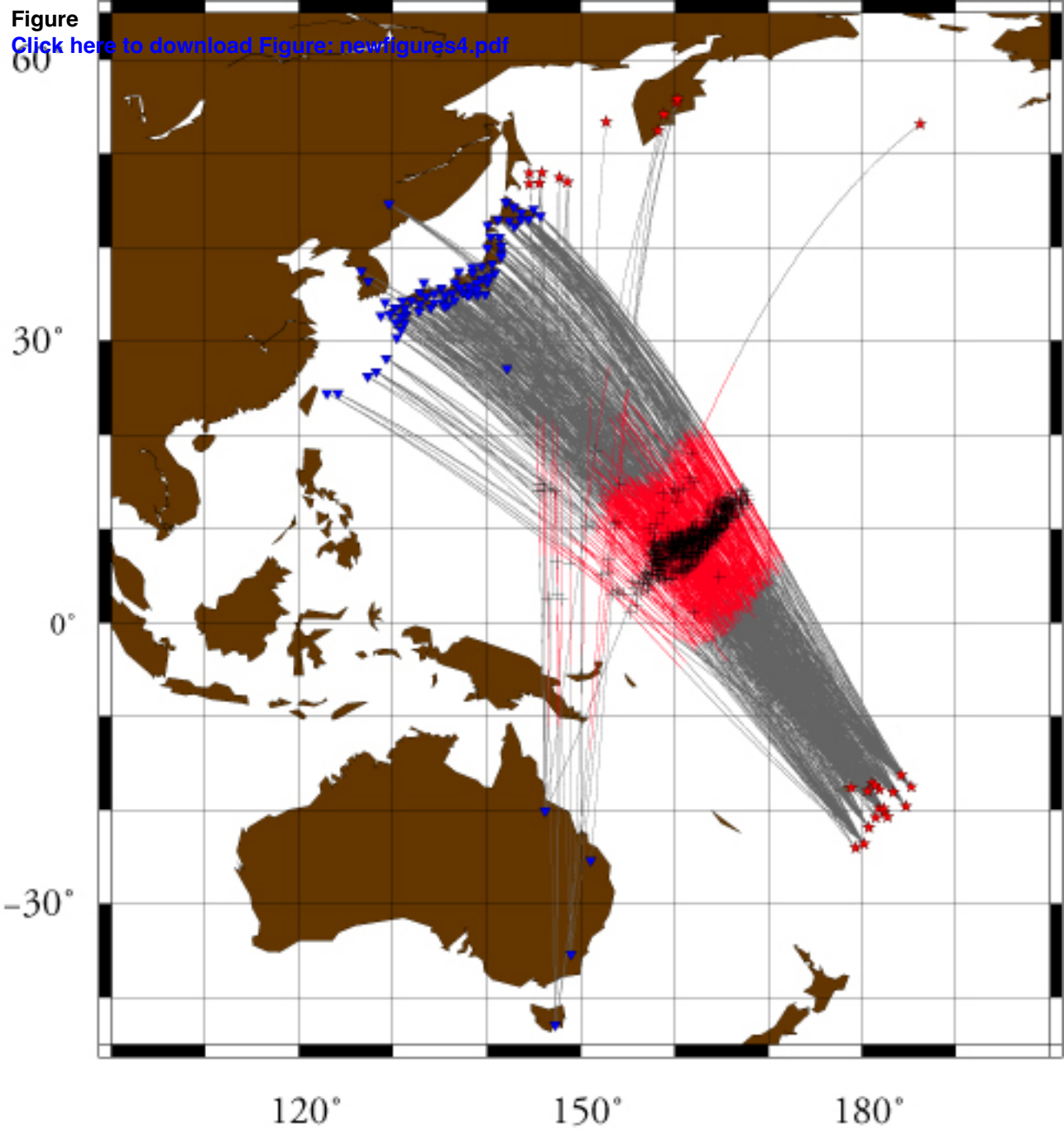

Fig. 1

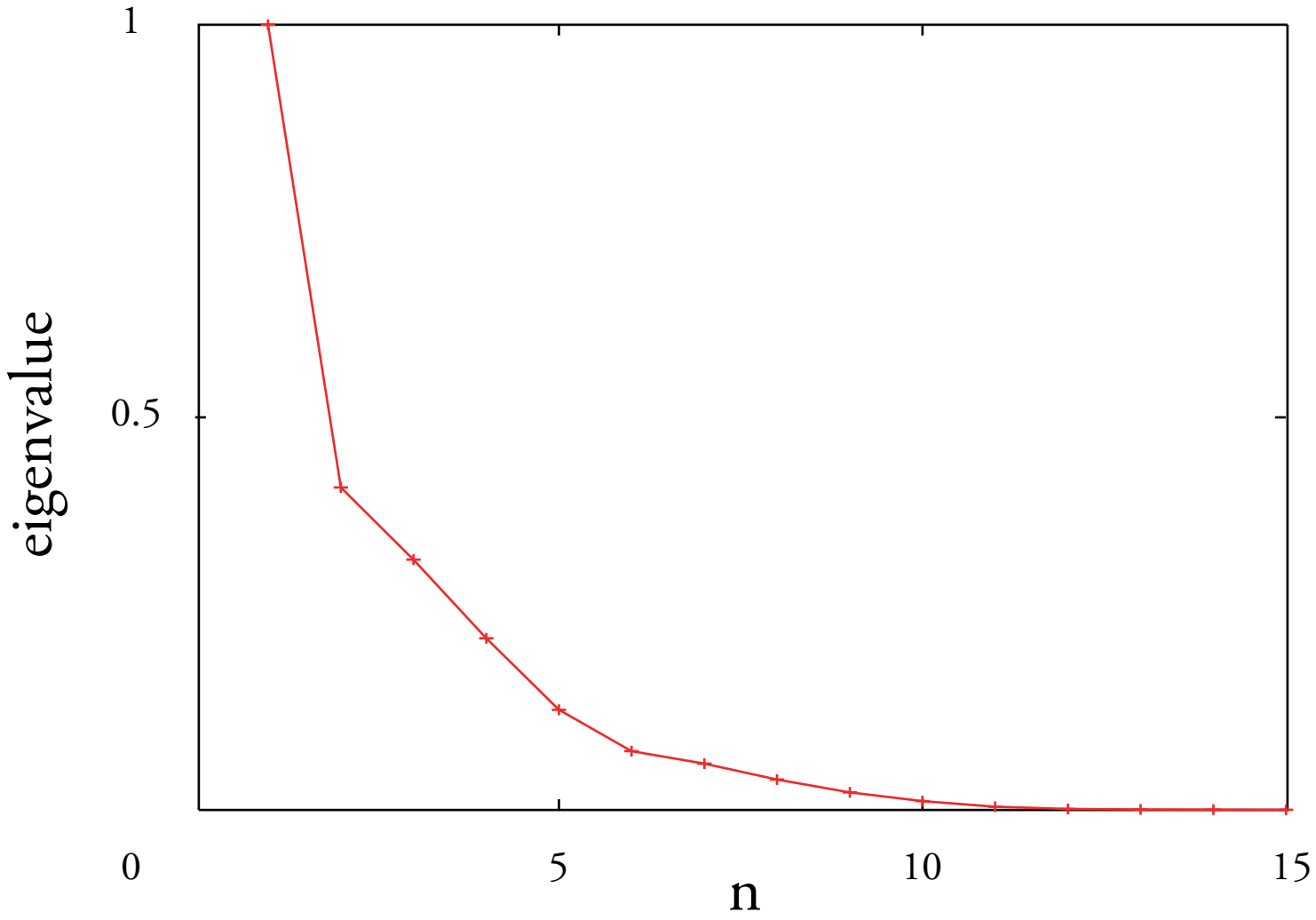
1
0.5
eigenvalue
0
5
10
15
n

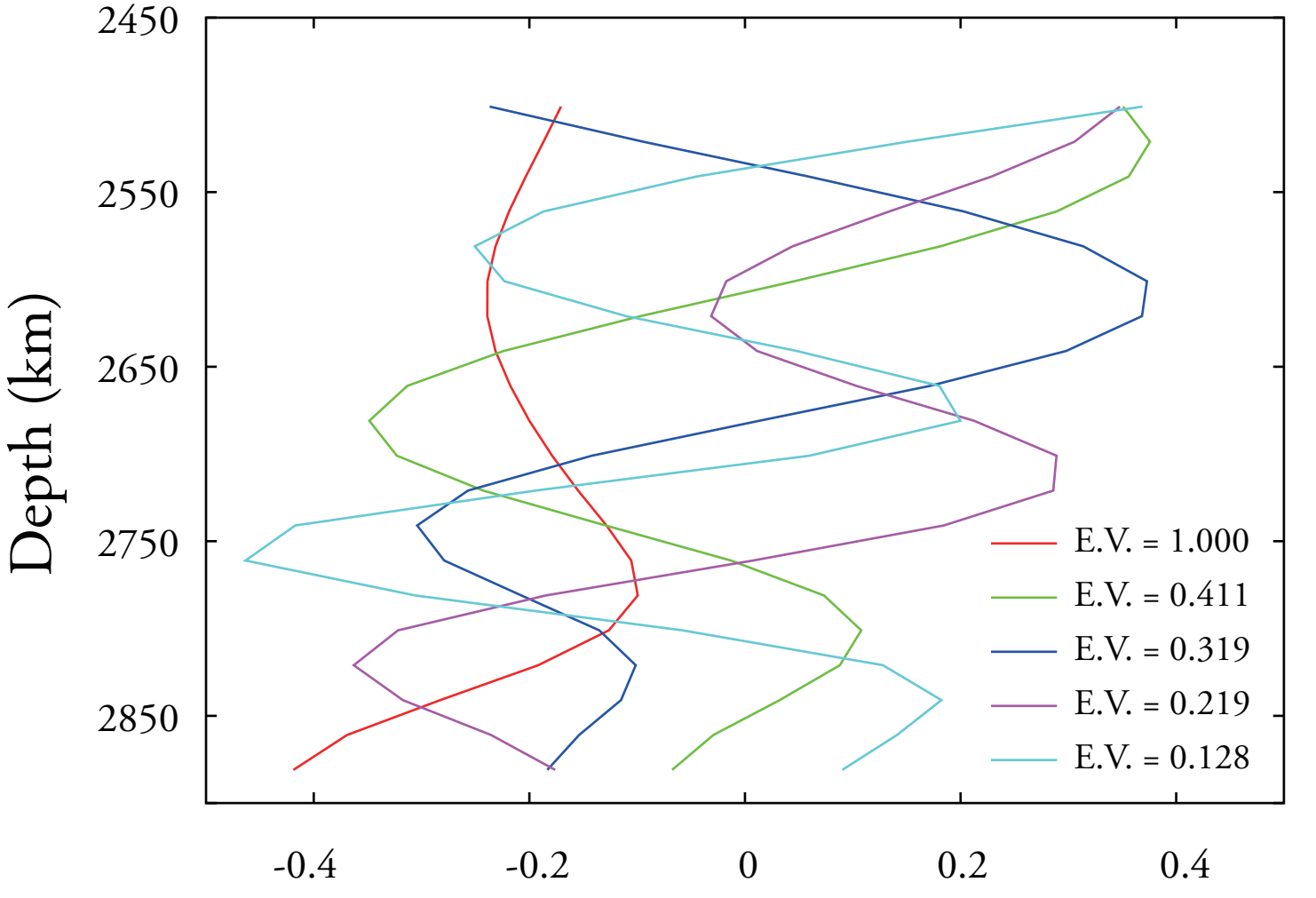
2450
2550
2650
2750
2850
Depth (km)
-0.4
-0.2
0
0.2
0.4
E.V. = 1.000
E.V. = 0.411
E.V. = 0.319
E.V. = 0.219
E.V. = 0.128

Fig 2

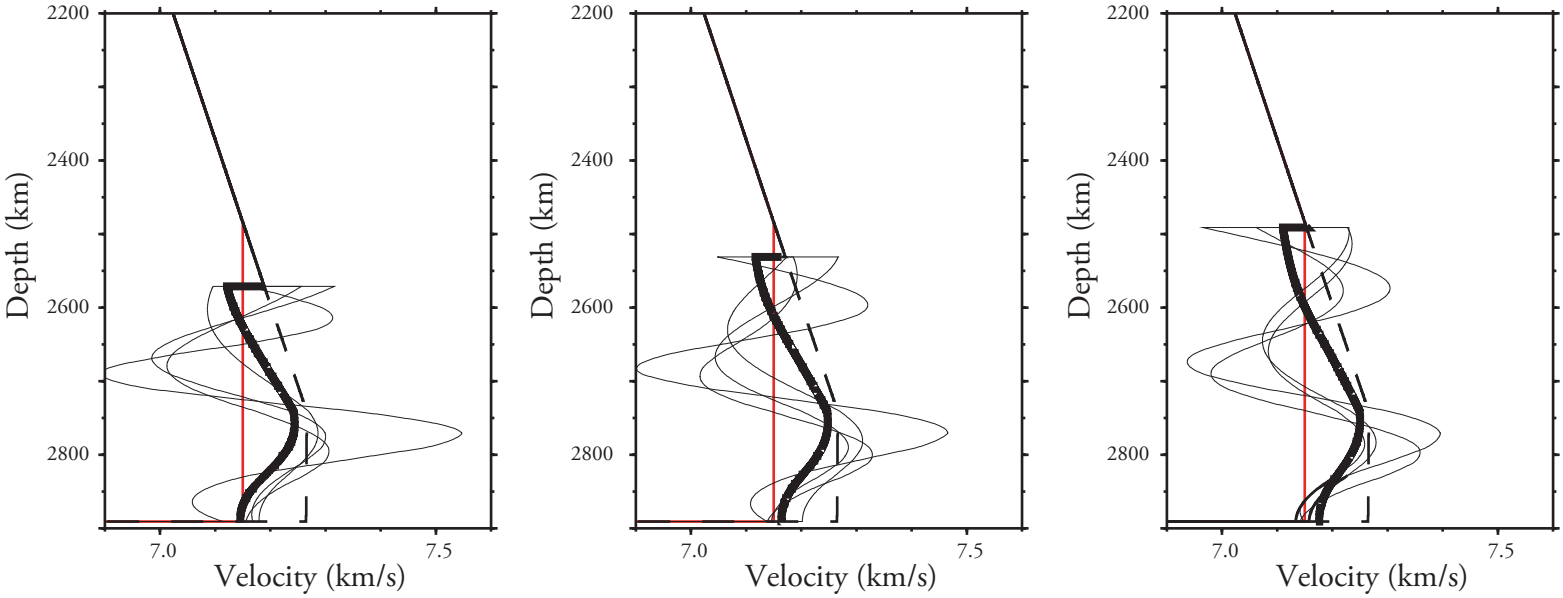
2200
2400
2600
2800
Depth (km)
7.0
7.5
Velocity (km/s)
2200
2400
2600
2800
Depth (km)
7.0
7.5
Velocity (km/s)
2200
2400
2600
2800
Depth (km)
7.0
7.5
Velocity (km/s)

Fig. 3

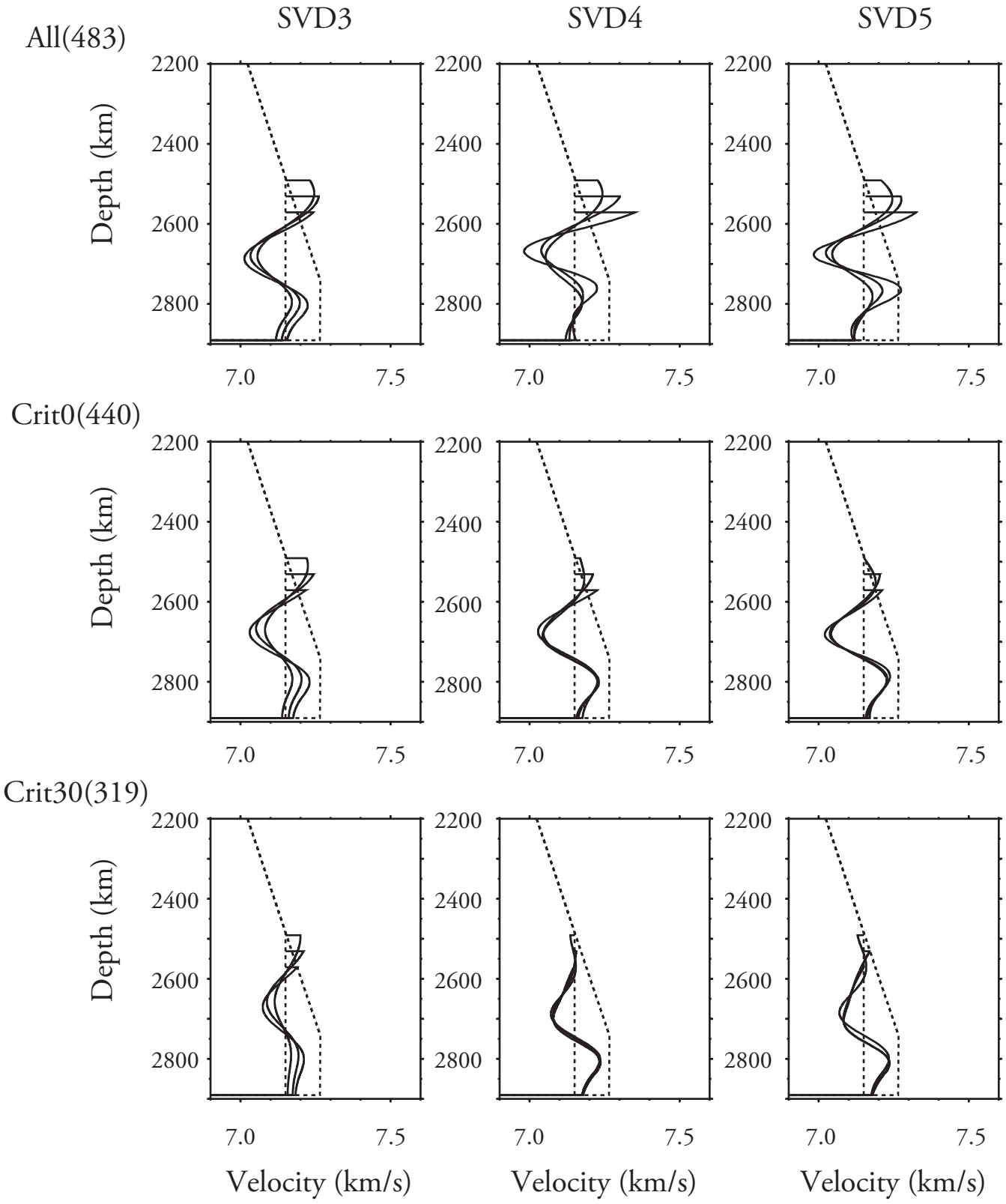
All(483)
SVD3
SVD4
SVD5
Crit0(440)
Crit30(319)
Depth (km)
2200
2400
2600
2800
7.0
7.5
Velocity (km/s)

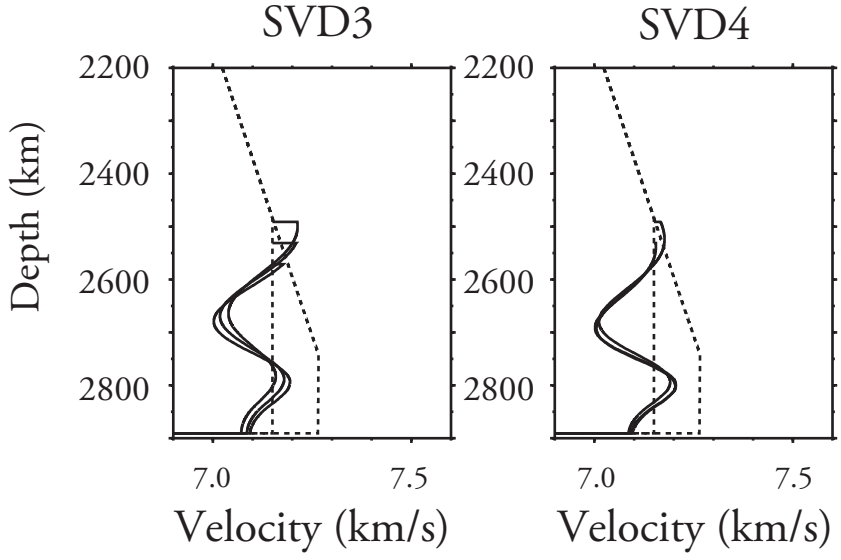
SVD3
SVD4
Depth (km)
2200
2400
2600
2800
7.0
7.5
Velocity (km/s)

Fig. 4

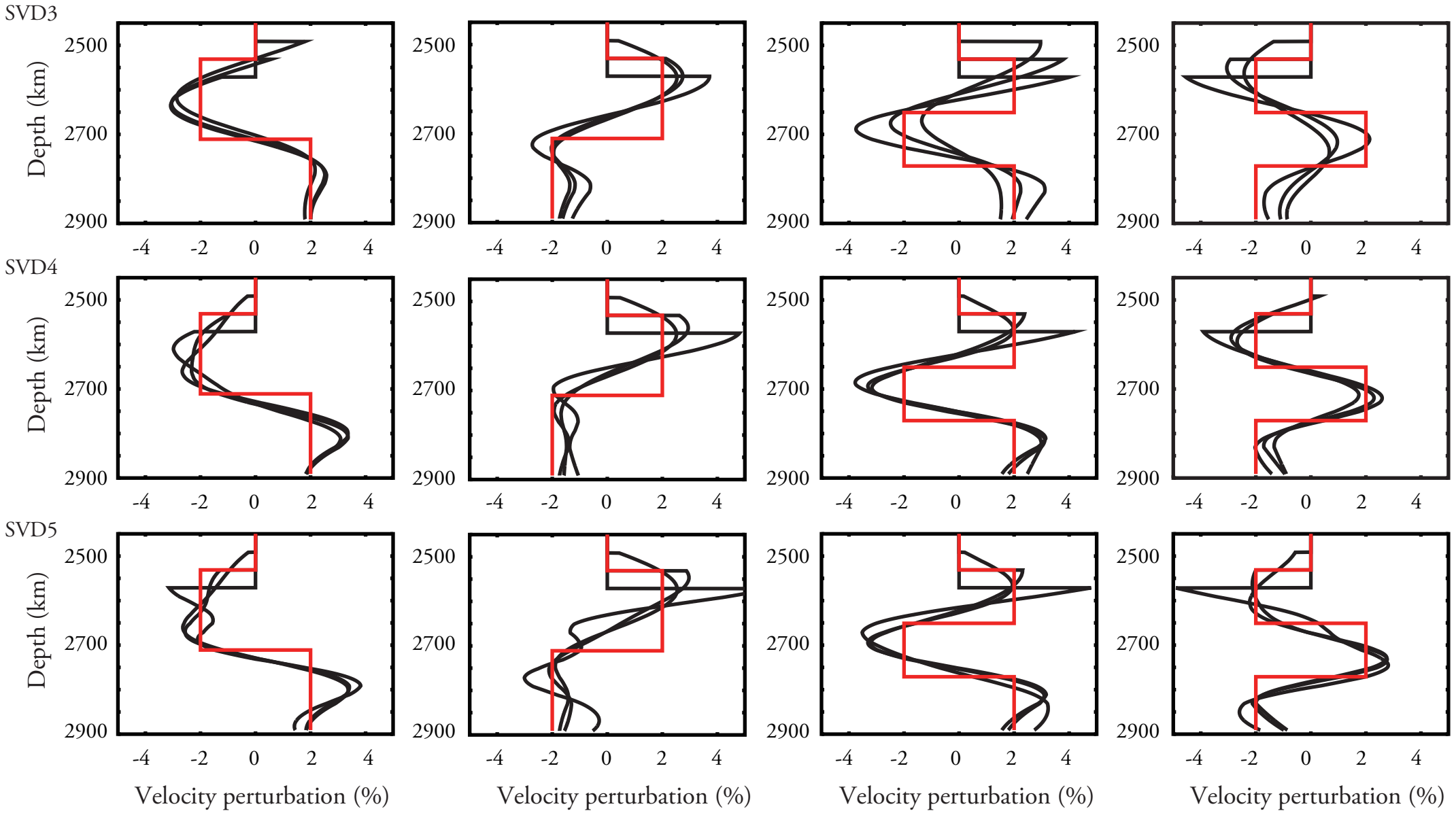
SVD3
SVD4
SVD5
Depth (km)
2500
2700
2900
-4
-2
0
2
4
Velocity perturbation (%)

Fig. 5

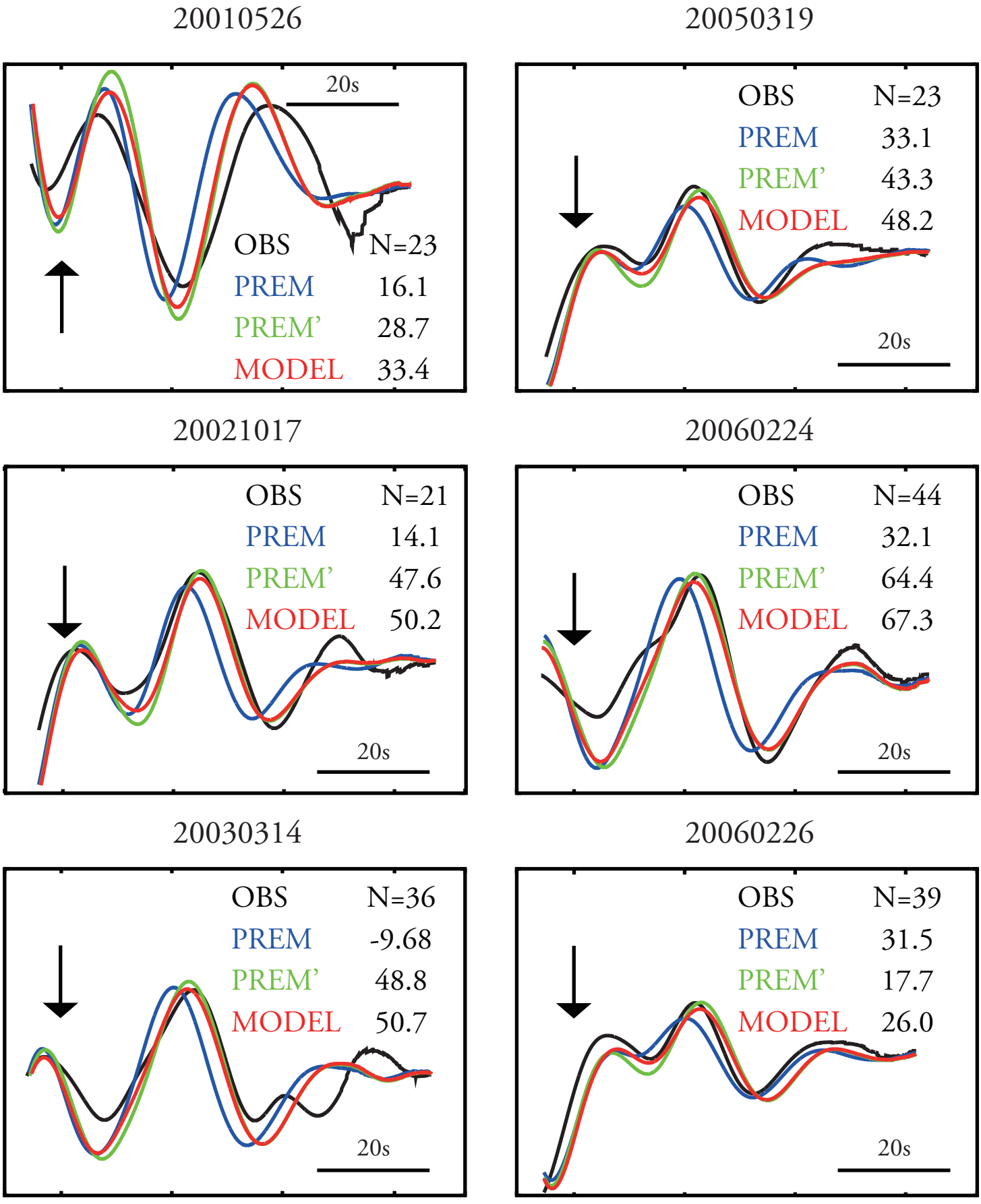
20010526
20s
OBS N=23
PREM 16.1
PREM' 28.7
MODEL 33.4
20050319
OBS N=23
PREM 33.1
PREM' 43.3
MODEL 48.2
20s
20021017
OBS N=21
PREM 14.1
PREM' 47.6
MODEL 50.2
20s
20060224
OBS N=44
PREM 32.1
PREM' 64.4
MODEL 67.3
20s
20030314
OBS N=36
PREM -9.68
PREM' 48.8
MODEL 50.7
20s
20060226
OBS N=39
PREM 31.5
PREM' 17.7
MODEL 26.0
20s

Fig. 6

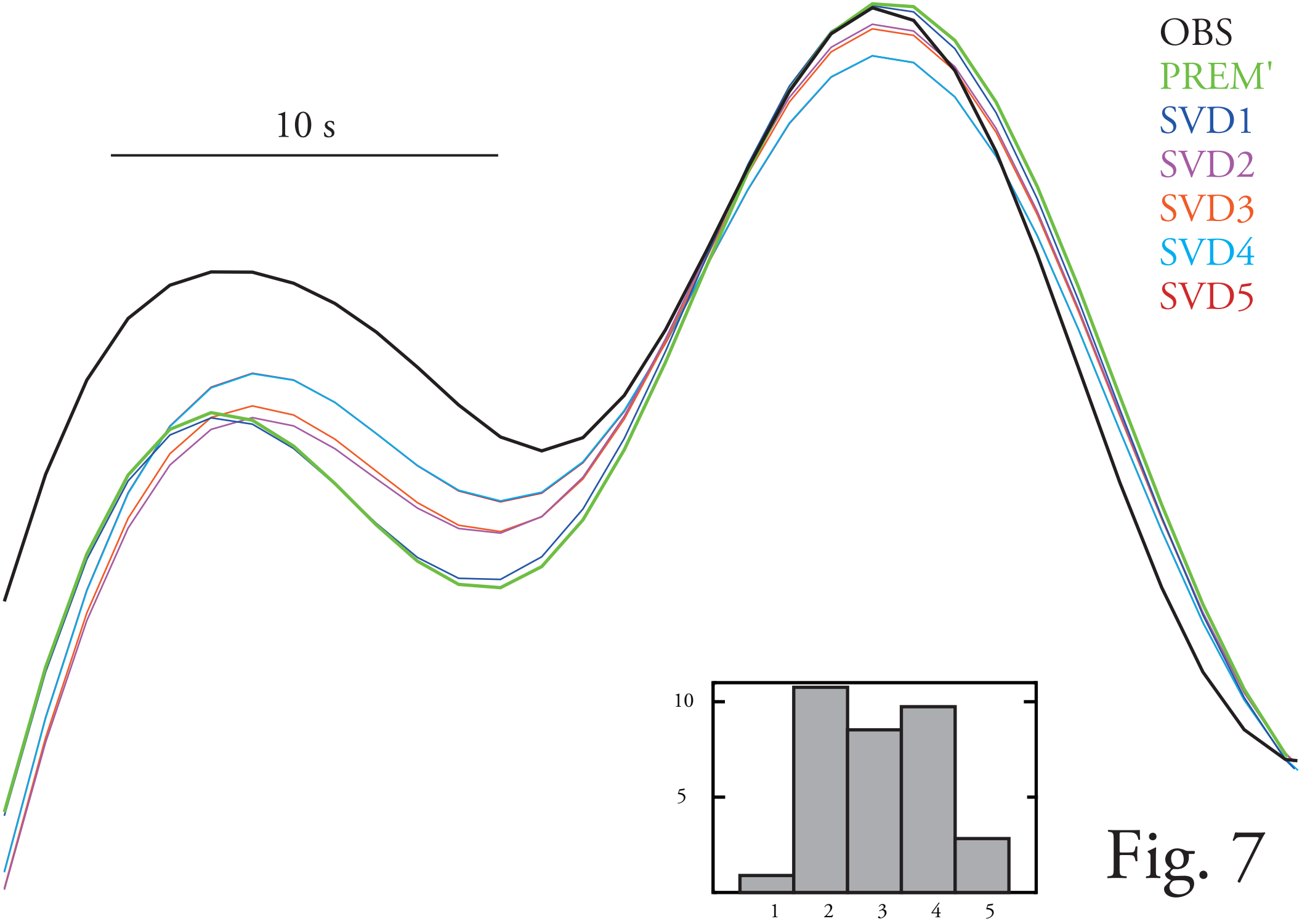

Fig. 7

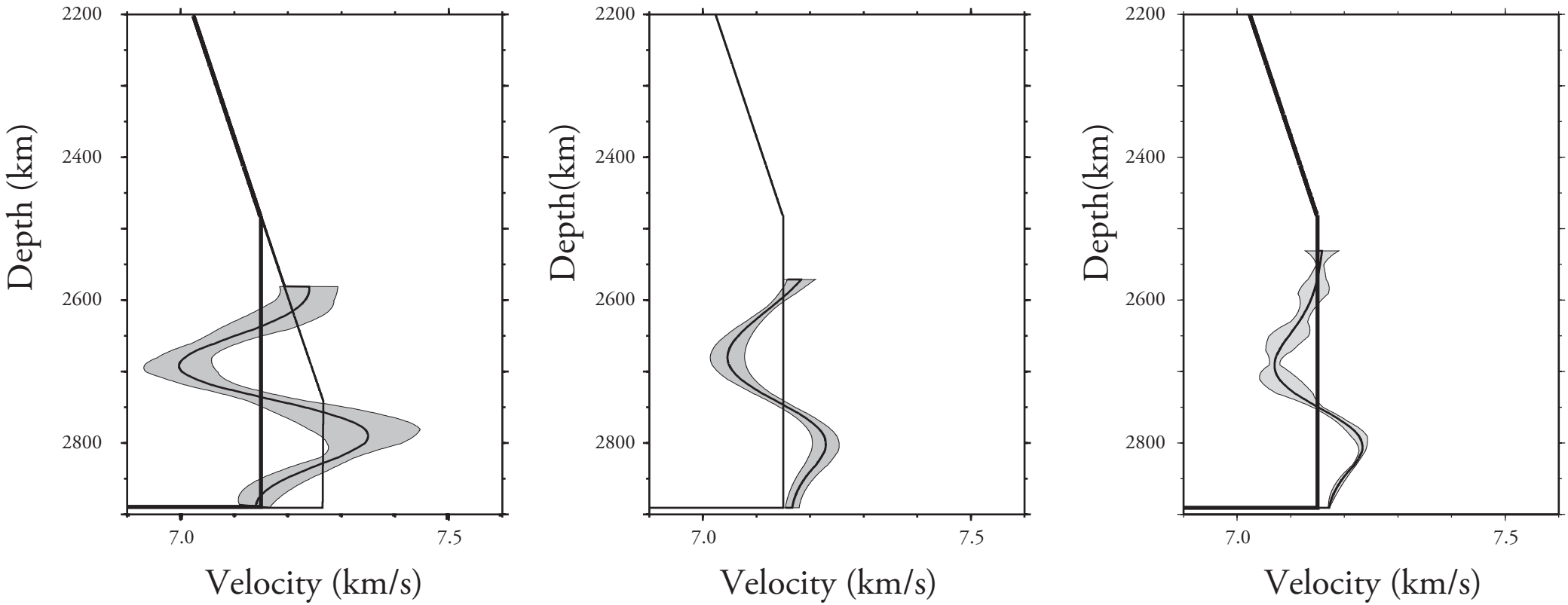
2200
2400
2600
2800
Depth (km)
7.0
7.5
Velocity (km/s)
2200
2400
2600
2800
Depth(km)
7.0
7.5
Velocity (km/s)
2200
2400
2600
2800
Depth(km)
7.0
7.5
Velocity (km/s)

Fig. 8